Electrochimica Acta 133 (2014) 254–261

Contents lists available at ScienceDirect

Electrochimica Acta

journal homepage: www.elsevier.com/locate/electacta

Preparation and Characterization of MnO_2/acid-treated CNT Nanocomposites for Energy Storage with Zinc Ions

Dongwei Xu[a,b], Baohua Li[a,*], Chunguang Wei[a,b], Yan-Bing He[a], Hongda Du[a], Xiaodong Chu[a], Xianying Qin[a], Quan-Hong Yang[a], Feiyu Kang[a,b]

[a] Engineering Laboratory for Next Generation Power and Energy Storage Batteries, Engineering Laboratory for Functionalized Carbon Materials, Graduate School at Shenzhen, Tsinghua University, Shenzhen 518055, China

[b] Laboratory of Advanced Materials, School of Materials,Tsinghua University, Beijing 100084, China

ARTICLE INFO

Article history:
Received 8 January 2014
Received in revised form 4 April 2014
Accepted 4 April 2014
Available online 13 April 2014

Keywords:
Manganese dioxide
Carbon nanotubes
MnO_2/CNT nanocomposites
Zinc ion storage
Rechargeable zinc ion battery

ABSTRACT

The rod-like manganese dioxide (MnO_2)/acid-treated carbon nanotube (a-CNT) nanocomposites have been synthesized by a simple co-precipitation method. The MnO_2 nanorod with the diameter of about 10 nm and length of 50∼120 nm is in-situ deposited on the surface of acid-treated CNT through the redox reaction of $KMnO_4$ and $Mn(CH_3COO)_2{\cdot}4H_2O$. Results show that the electron transfer efficiency of the MnO_2/a-CNT nanocomposites is greatly enhanced and results in a high electrical conductivity. The energy storage mechanism of as-prepared MnO_2/a-CNT in mild aqueous electrolyte ($ZnSO_4$ and $MnSO_4$) is associated with the insertion/extraction of zinc ion into/from the tunnels of crystalline α-MnO_2. The composites display both excellent storage properties with zinc ions (∼400 mAh·g^{-1} at 1 A·g^{-1}) and reversibility at various current rates (∼100% coulombic efficiency after 500 charge/discharge cycles). The MnO_2/a-CNT nanocomposites are rather promising cathode material for high performance rechargeable zinc ion batteries.

1. Introduction

An excellent energy storage device with ideal capacity, good reversibility, fast charge/discharge capability, safety, low cost and environmental friendliness is extremely desirable and important for this modern society. Various energy storage and conversion devices such as alkaline Zn/MnO_2 battery, lithium ion battery, lead–acid battery, nickel–cadmium battery and supercapacitor were extensively studied and used in our daily life [1–4]. However, existing aqueous batteries or power-type supercapacitors are far from achieving the final goals of an excellent energy storage application [1,5].

Due to the environmental benignity and low cost, MnO_2 and its composites have long been used as promising electrode materials in various energy devices such as primary Zn-MnO_2 battery [6], lithium ion battery [7] and supercapacitor [8]. Besides, a new secondary Zn/MnO_2 battery, made of α-MnO_2 as cathode, zinc metal as anode, and a mild zinc ion aqueous solution as electrolyte, was reported in our earlier work [5,9]. However, the mechanism of battery chemistries for secondary Zn/MnO_2 cell in mild aqueous electrolyte is different from that of the alkaline Zn/MnO_2 batteries, which is exposed to the so-called two-step (two-electron) pathways [10–12]. The energy storage of secondary Zn/MnO_2 cell is based on the insertion/extraction of zinc ions into/from the tunnels of crystalline α-MnO_2. At the anode, zinc electrode in a mild aqueous solution containing zinc ions is dissolved rapidly as Zn^{2+} ion during charge process and was deposited reversibly during discharging [13]. At the cathode, Zn^{2+} ions can be reversibly intercalated into and de-intercalated from the tunnels of α-MnO_2 in the same electrolyte system [14]. The mild Zn/MnO_2 battery can be used as a power-type reversible-battery with high capacity, safety, fast charge/discharge capability as well as environmental friendliness as compared with the primary Zn/MnO_2 batteries, supercapacitors and lithium ion batteries.

It is well-known that the basic crystalline structure of MnO_2 is constitutive of one manganese atom embraced by six oxygen atoms to form an octahedron. The MnO_6 octahedral subunits form crystalline tunnel structures by continuously linking to the neighboring subunits and sharing vertices and edges. There are various types of tunnel structures such as α-, β-, γ-, and δ-types that are classified into three groups according to the dimensions of tunnel structures in one, two, or three, respectively [15]. However, the electrical conductivity of MnO_2 is intrinsically poor. The key to its improvement is to add conductive additives to enhance the electron transport

* Corresponding author. Tel.: +755 2603 6419; fax: +755 2603 6419.
E-mail address: libh@mail.sz.tsinghua.edu.cn (B. Li).

http://dx.doi.org/10.1016/j.electacta.2014.04.001
0013-4686/

[16]. Because of excellent electrical conductivity and high specific surface area, carbon nanotube (CNT) is considered as an ideal material for MnO_2 to improve electrical conductivity. In recently published paper, the MnO_2/CNT composites have been prepared by following methods: mechanical mixing MnO_2 powder and carbon nanotube [17,18], the hydrothermal reaction of $KMnO_4$ and carbon nanotube [19], and the in-situ growth of MnO_2 in the multiwall carbon nanotube supported poly(3,4-ethylenedioxythiophene) [20]. Above composites were studied as the electrode materials for zinc ion batteries, lithium ion batteries and supercapacitors. A relatively high capacity could be achieved by depositing MnO_2 on the surface of the activated CNT due to the increase of the utilization ratio of MnO_2. Studies on CNT/metallic oxide and CNT/conducting polymer such as polypyrrole and PEDOT composite electrodes show that the CNT's surface area plays an important role for the increase of the material utilization, rate capabilities and electrode performance [20].

In this work, in order to further improve the performance of MnO_2 and increase the utilization ratio of MnO_2, the MnO_2 nanorod was in-situ deposited on the surface of the acid-treated CNT with negative charge to form MnO_2/CNT nanocomposites for zinc ion storage in a mild aqueous system. The negatively charged CNT after acid treatment easily attracted positively charged manganese metal and served as templates, which promotes the formation of MnO_2/CNT nano-structure with well dispersed CNT. The crystalline structure, composition and morphology of as-prepared MnO_2/CNT nanocomposites have been fully investigated. The synthesized MnO_2/CNT nanomaterial was used as the cathode material for the secondary Zn/MnO_2 battery in mild aqueous electrolyte. The mechanism of crystallographic forms of MnO_2 for Zn^{2+} ion storage has been also discussed.

2. Experimental

2.1. Materials synthesis

MnO_2-supported CNT nanocomposites were prepared by co-precipitation method with $KMnO_4$, $Mn(CH_3COO)_2{\cdot}4H_2O$, and CNT as the starting materials. Firstly, 0.25 g commercial multi-walled CNT with a diameter of 10∼20 nm and a length of 5∼13 um (Shenzhen Nanotech Port Co., Ltd., Shenzhen, China) were purified by refluxing the as-received sample in mixed acid (sulfuric acid: nitric acid = 3:1) for 6 h at 120 °C, and then dispersed in 20 mL deionized water by stirring for 0.5 h. Then, 1.69 g of the $Mn(CH_3COO)_2{\cdot}4H_2O$ was added into above suspension solution under continuously stirring for 0.5 h. Subsequently, the above mixed solution was added drop-wise into an aqueous solution prepared by dissolving 0.727 g $KMnO_4$ into 80 mL deionized water and stirring for 0.5 h. The mixed solution was then mixed intensively with a ultrasonic mixer for 10 min and heated for 6 h with oil bath controlled at a temperature of 80 °C. The dark brown precipitate thus formed was washed several times by deionized water and dried at 80 °C in air for 24 h to finally obtain the MnO_2/acid-treated CNT nanocomposites (marked as MnO_2/a-CNT). For comparison, the MnO_2/original CNT composites were also synthesized following the above procedure with original CNT (marked as MnO_2/o-CNT).

2.2. Material characterization

The crystallographic characteristics of the acid-treated CNT and the MnO_2/CNT nanocomposites were characterized by X-ray diffraction (XRD) using Rigaku 2500 powder diffractometer (Cu Kα radiation, λ=1.54056 Å). The diffraction patterns were recorded over the 2θ angle of 10∼80° at 40 kV, 30 mA with a step size of 0.02°. The morphologies of the sample were observed by field emission scanning electron microscopy (SEM) of HITACHI S4800 at 5 kV and high-resolution transmission electron microscopy (HRTEM) of FEI TECNAI G^2 at 300 kV. The thermogravimetric analysis (TGA) and different scanning calorimetry (DSC) was carried out on a Mettler Toledo TGA thermogravimetric analyzer with heating rate of 10 °C·min^{-1} from 50 °C to 900 °C in the air. The fourier transform infrared spectroscopy (FT-IR) analysis was conducted with a vertex-70 (BRUKER, Germany) in the spectral range from 4000 to 500 cm^{-1}. X-ray photoelectron spectroscopy (XPS) was conducted with a Physical Electronics PHI5802 instrument using X-rays magnesium anode (monochromatic Kα X-rays at 1253.6 eV) as a source, which was employed to evaluate the valence change of Mn during charge and discharge of the MnO_2/CNT nanocomposites. The Zn/Mn molar ratio of MnO_2/CNT electrodes was analyzed by an ICAP6300 inductively coupled plasma optical emission spectrometer (ICP-OES) (Thermal, USA).

2.3. Electrochemical characterization

The electrochemical performance of the MnO_2/CNT nanocomposites was tested using a CR2032-type coin cell. In order to prepare cathode, the as-prepared MnO_2/CNT powders, carbon black, LA133 water-based adhesives and carboxymethyl cellulose (CMC) were mixed with a weight ratio of 70:20:8:2 using deionized water. The mixed slurry was coated on steel foil (30 um) and dried at 80 °C under vacuum for 12 h. The anode is composed of 80 wt.% zinc powder, 10 wt.% activated carbon, 8 wt.% LA133 water-based adhesives and 2 wt.% CMC, which were coated on zinc foil and dried at 80 °C for 12 h under vacuum. The MnO_2/CNT as a research electrode was the limiting reagent, while the zinc anode as counter electrode is excess in order to adequately play the performance of MnO_2/CNT cathode. The 2 mol·L^{-1} $ZnSO_4$ and 0.5 mol·L^{-1} $MnSO_4$ hybrid aqueous solution was used as electrolyte. The separator is the sulfonated membrane on the side of cathode and the filter paper on the side of anode. The cyclic voltammetry test was carried out using a VMP3 multichannel electrochemical station (Bio-Logic-Science Instruments SA, France) with potential range from 1.0 V to 1.9 V versus Zn/Zn^{2+}. The rate cyclic performance was tested at a constant current mode with various charge and discharge rates using a LAND CT2001 apparatus (China). All the electrochemical measurements were carried out at room temperature.

3. Results and Discussion

3.1. Physicochemical characterizations

Fig. 1 shows the crystal structures of the as-prepared MnO_2/a-CNT nanocomposites and the acid-treated CNT by XRD characterization. The XRD pattern of the acid-treated CNT displays four diffraction peaks at 25.9°, 42.8°, 53.6° and 78.0°, which can be indexed as (002), (100), (004) and (110) reflections of graphite, respectively [21–23]. For the MnO_2/a-CNT sample, the intensive peaks appeared at 12.6°, 17.7°, 28.3°, 37.2°, 41.6°, 49.5°, 59.6°, 65.3° and 68.6°, respectively, should be ascribed to the characteristic peaks of α-MnO_2 (JCPDS 44-0141) [24–26]. The tunnel size of α-MnO_2 is 4.6 Å, which is suitable for insertion/extraction of alkali cations [15]. Moreover, the average particle size of as-prepared MnO_2/a-CNT material is 9.8 nm calculated by XRD pattern. Besides, the peak occurred at 25.9° should be assigned to the (002) planes of graphite carbon, which indicates the presence of carbon nanotube in the MnO_2/a-CNT nanocomposites.

Thermogravimetric analysis (TGA) was used to examine the percent of MnO_2 in MnO_2/a-CNT. Fig. S1 shows the DSC and TG curves of MnO_2/a-CNT. The weight loss of sample below 340 °C is ∼8 wt%, which may result from the removal of minor water and functional

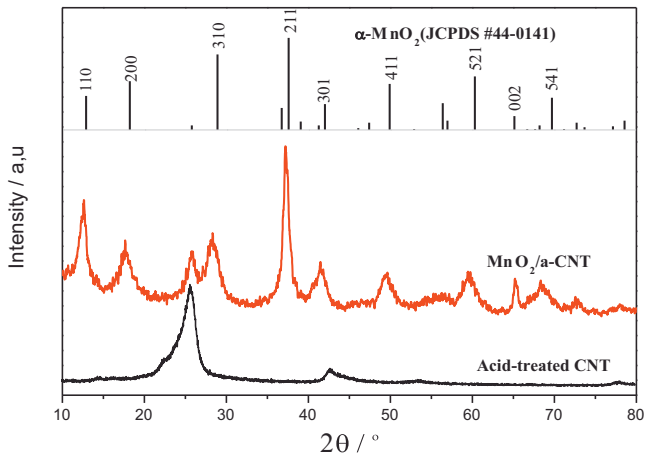

Fig. 1. XRD patterns of the MnO_2/a-CNT nanocomposites and the acid-treated CNT.

group (carbonyl, carboxyl and hydroxyl group). The weight loss in the temperature range of 340∼500°C is ∼18 wt%, which is corresponding to a large exothermic peak in DSC curve. Because the structure of MnO_2 is stable below 500 °C [27]. The weight between 340 and 500°C is due to the burning of CNT. It is obtained that the percent of MnO_2 in MnO_2/a-CNT is ∼74 wt%.

Fig. 2(a) is the SEM image of the acid-treated CNT, revealing the regular morphology with external diameter of 20∼40 nm. FT-IR of the original and acid-treated CNT was tested and their corresponding spectra are shown in Fig. 2(b). For the original CNT, the IR spectrum shows an important absorption band at 3454 cm^{-1} (attributed to OH stretching), which may result from oxidation during the purification of the raw material and/or ambient atmospheric moisture [28]. After the acid treatment, the intensity of OH stretching absorption band (at 3447 cm^{-1}) obviously increased, and the large new peaks appeared at 1715 cm^{-1} (assigned to C = O stretching), 1580 cm^{-1} (assigned to–COO–asymmetric stretching) and 1218 cm^{-1} (attributed to C-O stretching), which indicate the introduction of rich oxygen-containing functional group such as carbonyl, carboxyl and hydroxyl group during the acidification process of carbon nanotube. The above observation is consistent with the following result of oxygen content measured by EDS. Fig. S2 and Fig. 2(c-d) show the EDS images of the original and acid-treated CNT, respectively. The elemental analysis indicates that the oxygen content in acid-treated CNT (15.6 wt%) is much higher than that of original CNT (5.3 wt%), which manifests the introduction of oxidative functional groups in the acidization process. The functionalization of CNT can increase the active sites, which contribute to the combination between MnO_2 and CNT in the preparation process of MnO_2/a-CNT material. Moreover, the impurities such as Si and Ni in original CNT were removed after the acid treatment.

The morphology and dimension of the as-prepared MnO_2/a-CNT nanocomposites are shown in Fig. 3. As shown in Fig. 3(a) and (c), there was tortuous tube type of the acid-treated CNT in the synthetic MnO_2/a-CNT nanocomposites, compared with solid-stem straight type of the nanorod MnO_2 particles that covered over the acid-treated CNT's surface. In order to indentify whether the acid-treated CNT was uniformly dispersed in MnO_2 nanowire, EDS and elemental mapping of MnO_2/a-CNT nanocomposites were examined and shown in Fig. 3(b). The EDS result reveals that the MnO_2/a-CNT nanocomposites contain ∼20 wt% of C, which is roughly in agreement with the result of thermogravimetric analysis. From the elemental mapping images of Mn, O and C for the as-prepared MnO_2/a-CNT nanocomposites, it is seen that not only the elements of Mn and O are uniformed distributed, but also the C element is homogeneously dispersed in the MnO_2/a-CNT nanocomposites, indicating the formation of a uniform three-dimensional CNT network. Furthermore, the HRTEM images in Fig. 3(c-d) clearly

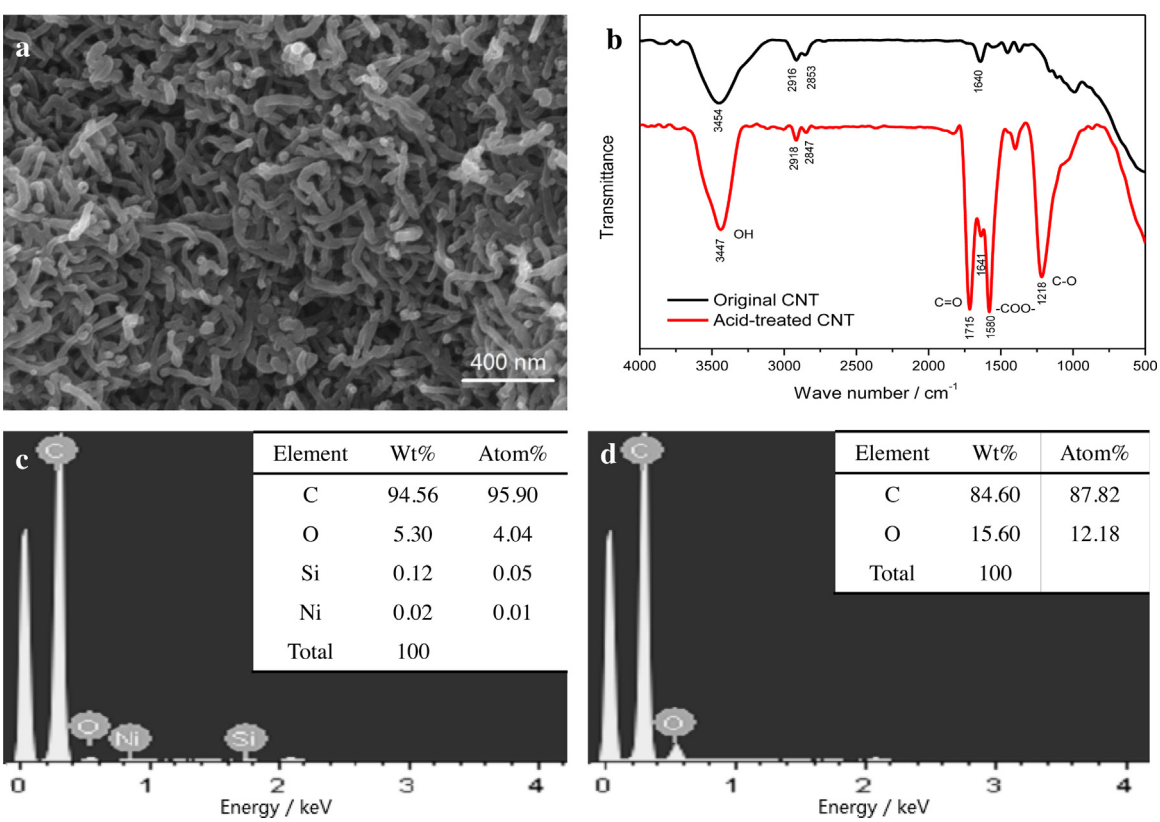

Fig. 2. SEM image of acid-treated CNT (a); FT-IR spectra of the original and acid-treated CNT (b); EDS images of the original CNT (c) and acid-treated CNT (d).

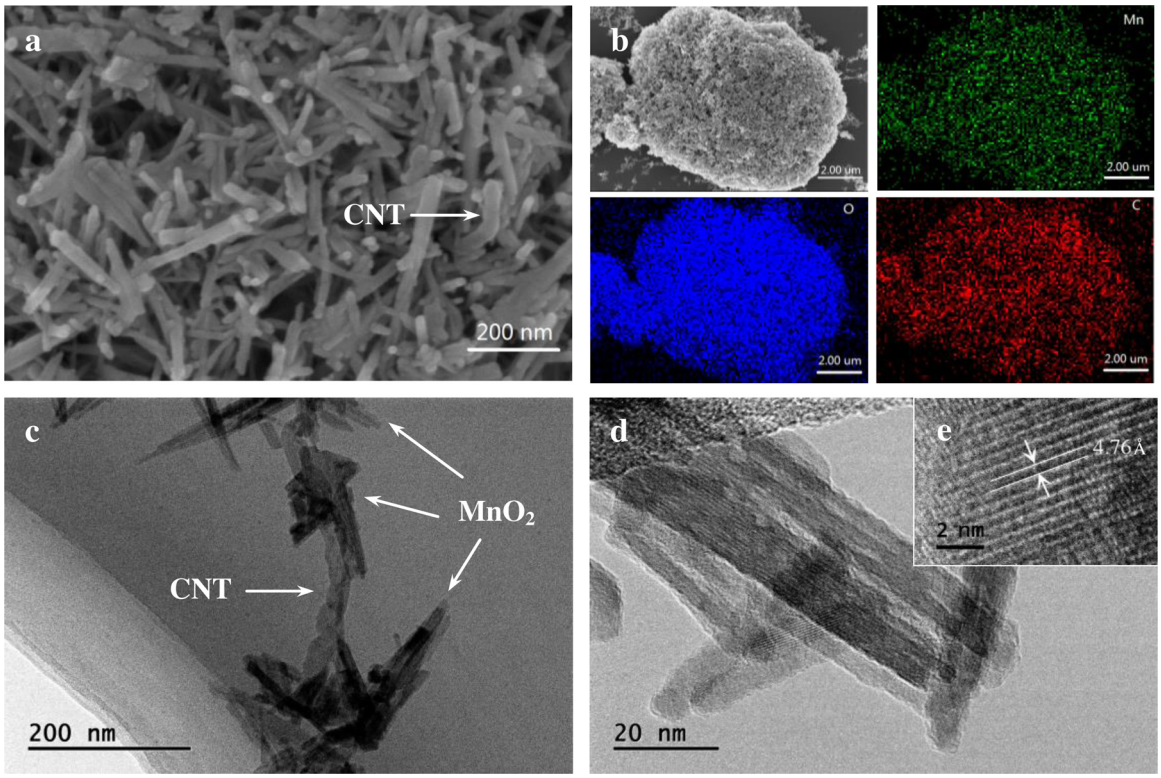

Fig. 3. SEM image of the MnO_2/a-CNT nanocomposites (a); EDS mappings of Mn, O and C elements of the MnO_2/a-CNT nanocomposites (b); HRTEM patterns of the MnO_2/a-CNT nanocomposites (c-e).

shows that the rod-like MnO_2 have the diameter of about 10 nm and length of 50∼120 nm, which is the same as the result of analysis by XRD. The HRTEM image of the α-MnO_2 nanorods as given in Fig. 3(e) shows a clear lattice structure with D-spacing of 4.76 Å, corresponding to the (200) crystal plane of α-MnO_2.

3.2. Electrochemical properties

MnO_2 has usually been used energy storage material for all kinds of energy devices, for example, primary Zn-MnO_2 batteries [6], lithium ion batteries [7] and supercapacitors [29]. It has been reported that MnO_2 can exhibit an ideal capacitive performance in the neutral electrolytes containing alkaline (Li^+, Na^+ or K^+) and alkaline-earth (Mg^{2+}, Ca^{2+} or Ba^{2+}) metal cations [8,25,29,30]. There are two mechanisms to explain the ions storage behavior of MnO_2. For Li^+, Na^+, K^+ or H_3O^+, the first mechanism involves the intercalation/extraction of protons (H_3O^+) or alkali cations, which can be described by the following equation [15,26,31]:

$$MnO_2 + M^+ + e^- \leftrightarrow MnOOM(M^+ = Li^+, Na^+, K^+ \text{or} H_3O^+) \quad (1)$$

The other mechanism is based on the adsorption process on the surface of MnO_2 as follow [15,32]:

$$(MnO_2)_{surface} + M^+ + e^- \leftrightarrow (MnOOM)_{surface}(M^+ = Li^+, Na^+, K^+ \text{or} H_3O^+) \quad (2)$$

Similar equations can be written readily for Zn^{2+}, Mg^{2+}, Ca^{2+} or Ba^{2+}.

Our previous work found that the insertion/extraction behavior of zinc ion for α-MnO_2 is fast and reversible [5,9,15]. According to this study, the prepared MnO_2/CNT nanocomposites show the good cycling property, high capacity and fast reversibility. Their zinc ion storage property was also investigated in following content.

Electrochemical Zn^{2+} insertion/extraction properties of the MnO_2/a-CNT nanocomposites was evaluated by the cyclic voltammogram (CV) and the galvanostatic charge/discharge tests in the voltage range of 1.0 V∼1.9 V vs. Zn/Zn^{2+}. Fig. 4(a) shows the CV curve (the tenth cycle) of the MnO_2/a-CNT electrode in 2 mol·L^{-1} $ZnSO_4$ and 0.5 mol·L^{-1} $MnSO_4$ hybrid aqueous electrolyte at a sweep rate of 0.5 mV·s^{-1}. Two distinguishable peaks were emerged at around 1.6 V and 1.35 V during charge/discharge process, respectively. This redox couple should be associated with the insertion/extraction of Zn^{2+} ions into/from the tunnel of MnO_2 nanocomposites. The reduction reaction equation of Zn^{2+} can be described as the equation (3). The concentration of Zn^{2+} in the neutral aqueous solution system used in this study is 2 mol·L^{-1}. According to the nernst equation, the Zn equilibrium potential in above solution is -0.75 V. Moreover, because the reaction mechanism of Zn^{2+} insertion into MnO_2 is described as the equation (4), which is similar with the equation (5). Thus, the potential of Zn^{2+} insertion into MnO_2 should be around +0.95 V. In addition, the polarization behavior of electrode during CV test also influences the Ox-Re potential change and result in the increase of oxidation peak potential and decrease of reduction peak potential of MnO_2/a-CNT electrode. Therefore, we observed two ox-re peaks at 1.35 V and 1.60 V, respectively. The potential difference between oxidation peak and reduction peak of MnO_2/a-CNT electrode is about 0.25 V, which indicates that the Zn^{2+} insertion-extraction process can be regarded as quasi-reversible behavior [9].

$$Zn^{2+}(aq) + 2e^- \rightarrow Zn(s)(-0.76\,V) \quad (3)$$

$$2MnO_2(s) + Zn^{2+} + 2e^- \rightarrow ZnMn_2O_4(s) \quad (4)$$

$$2MnO_2(s) + 2e^- \rightarrow Mn_2O_4{}^{2-}(aq)(+0.95\,V) \quad (5)$$

The MnO_2/a-CNT electrodes in original, extraction (potentiostated at 1.6 V) and insertion (potentiostated at 1.35 V) states were studied by XRD and XPS analyses. The XRD patterns of

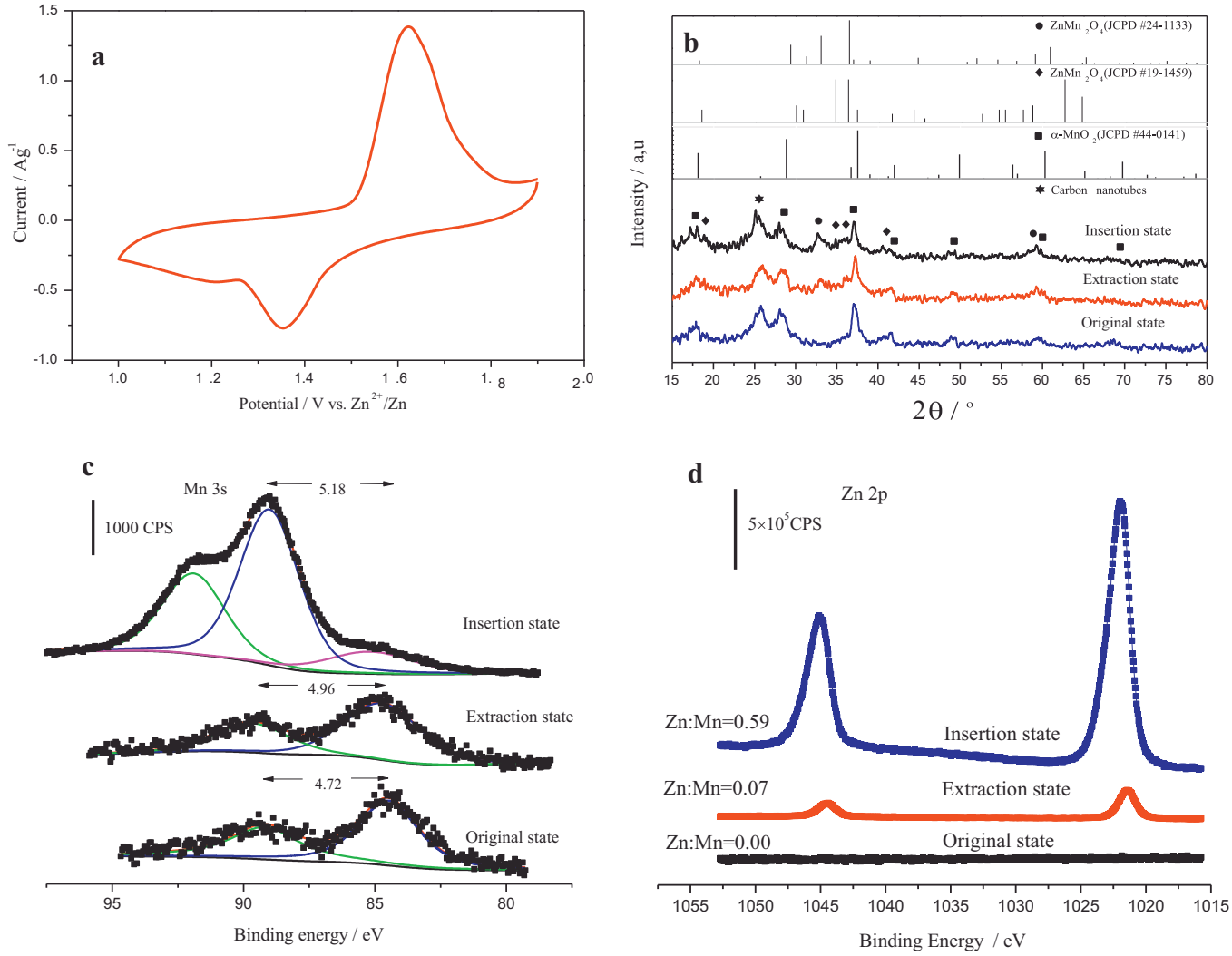

Fig. 4. CV curve (the tenth cycle) of the MnO_2/a-CNT electrode in 2 mol·L^{-1} $ZnSO_4$ and 0.5 mol·L^{-1} $MnSO_4$ hybrid aqueous electrolyte at a sweep rate of 0.5 mV·s^{-1} (a), XRD patterns of MnO_2/a-CNT electrodes in the original, extraction and insertion states (b), Mn 3s (c) and Zn 2p (d) core level spectra of MnO_2/a-CNT electrodes in the original, extraction and insertion states, The raw data are represented by the dots, and the fitted data are represented by the lines.

MnO_2/a-CNT electrodes in original, extraction and insertion states are shown in Fig. 4(b). The formation of $ZnMn_2O_4$ in the insertion state proves that zinc ions have been inserted into crystal of MnO_2, which may result from the presence of the tunnel in α-MnO_2. In the extraction state, however, the most of α-MnO_2 is similar to the original state. It can be seen that the electrochemical insertion/extraction behavior of Zn^{2+} ion into/from MnO_2 are quite different from a capacitive behavior, and such difference cannot be explained on the account of the ion size with the radius at 0.74, 0.69, 1.02, and 1.38 nm for Zn^{2+}, Li^+, Na^+, and K^+, respectively [9]. This result is supported by XPS analysis of the MnO_2/a-CNT electrodes in the mild aqueous electrolyte (Fig. 4(c-d)).

The Mn 3s core level spectra usually shows a peak splitting and a doublet, owing to the parallel spin coupling of 3s electron within the 3d electron during the photoelectron ejection. Such an interchange occurs as a representative multiplet splitting between electrodes in the 3s-3d level of manganese, and the graphical representation of the separation of peak energies (ΔE) in the exchange interaction energy is expressed by equation (6):

$$\Delta E = (2S + 1)K[3s, 3d] \quad (6)$$

where S is the total spin of unpaired electrons in the 3s and 3d levels in the final states and K[3s,3d] is the exchange integral between 3s-3d energy levels. Therefore, the splitting of the 3s peak becomes wider when the valence of Mn in the oxide decreases because of fewer unpaired electrons in the 3d level [32–34]. Fig. 4(c) shows the Mn 3s core-level spectra of MnO_2/a-CNT cathodes in the original, extraction and insertion states. The separations of peak energies of the Mn 3s components are 4.75, 4.96 and 5.18 eV, respectively, for the original, extraction and insertion states. From equation (6), the average valences of Mn in the original, extraction and insertion states are calculated to be 4.08, 3.69 and 3.28 respectively. Consequently, it was clear that a change of the separation of peak energies for the Mn 3s occurred in the charge/discharge process, which indicates that the extraction state of Mn decreased from positive quadrivalent to positive trivalent for the insertion state. Moreover, as shown in Fig. 4(d), the result of Zn 2p core level spectra of MnO_2/a-CNT electrodes in original, extraction and insertion states is the same as that of Mn 3s core level spectra. When the MnO_2/a-CNT electrode is in a state of insertion, its intensity of Zn 2p core level spectra is higher than the original and extraction states. And the molar ratio of Zn/Mn in original, extraction and insertion states is 0.00, 0.07 and 0.59 by the analysis of ICP-OES. The augment intensity of Zn 2p from extraction to insertion states clearly confirms the insertion/extraction of Zn^{2+} ion into/from α-MnO_2. In accordance with electrochemical and physical characterizations,

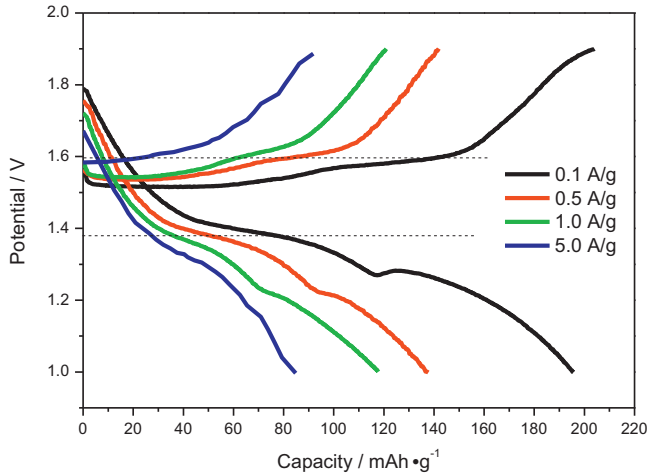

Fig. 5. The charge/discharge curves (the fifth cycle) of the MnO_2/a-CNT electrode in 2 mol·L^{-1} $ZnSO_4$ and 0.5mol·L^{-1} $MnSO_4$ hybrid aqueous electrolyte.

the insertion/extraction of zinc ion into/from the tunnels of crystalline α-MnO_2, as occurred during the charge/discharge process in the mild aqueous electrolyte, can be described by equation (4).

The charge/discharge curves of the MnO_2/a-CNT electrode in 2 mol·L^{-1} $ZnSO_4$ and 0.5 mol·L^{-1} $MnSO_4$ hybrid aqueous electrolyte at the current densities of 0.1 A·g^{-1}, 0.5 A·g^{-1}, 1.0 A·g^{-1} and 5.0 A·g^{-1} are shown in Fig. 5, respectively. It is seen that the charge and discharge plateaus of the Zn-MnO_2/a-CNT battery in the mild electrolyte emerge at around 1.6 V and 1.38 V under various current densities, which have minor increase (charge plateau) and decrease(discharge plateau) with the current densities increase from 0.1 to 5 A·g^{-1}. On the basis of electrochemical measurements, the performance of MnO_2/a-CNT electrode for the storage of Zn^{2+} in the mild electrolyte shows a reversible-battery behavior, similar to lithium ions battery [11,35].

The electrochemical performance of the MnO_2/a-CNT and MnO_2/a-CNT electrodes at various current densities were studied and compared (Fig. 6). It is found that the specific capacity of MnO_2/a-CNT is much larger than that of the MnO_2/o-CNT material. It follows that the purification and functionalization of CNT are of very importance for the improvement of the electrochemical performance of MnO_2/CNT nanocomposites. In addition, the specific capacity of MnO_2/a-CNT firstly increased and then maintained steady after a period of time, with the increase of cycling number. The discharge capacity finally maintained steady at 665 mAh·g^{-1}, 540 mAh·g^{-1}, 400 mAh·g^{-1} and 100 mAh·g^{-1} for the current density of 0.1A·g^{-1}, 0.5 A·g^{-1}, 1A·g^{-1} and 5A·g^{-1} respectively, which are at least twice as much as those of the primary alkaline Zn/MnO_2 batteries and the lithium ion batteries [5,36,37].

The MnO_2/a-CNT nanocomposites display both excellent zinc ion storage property and high reversibility at various current densities, which may result from the in-situ growth of MnO_2 nanomaterial on the uniform three-dimensional functional CNT network. In detail, the acid-treated CNT contains large surface and rich oxygen-containing functional groups such as carboxyl

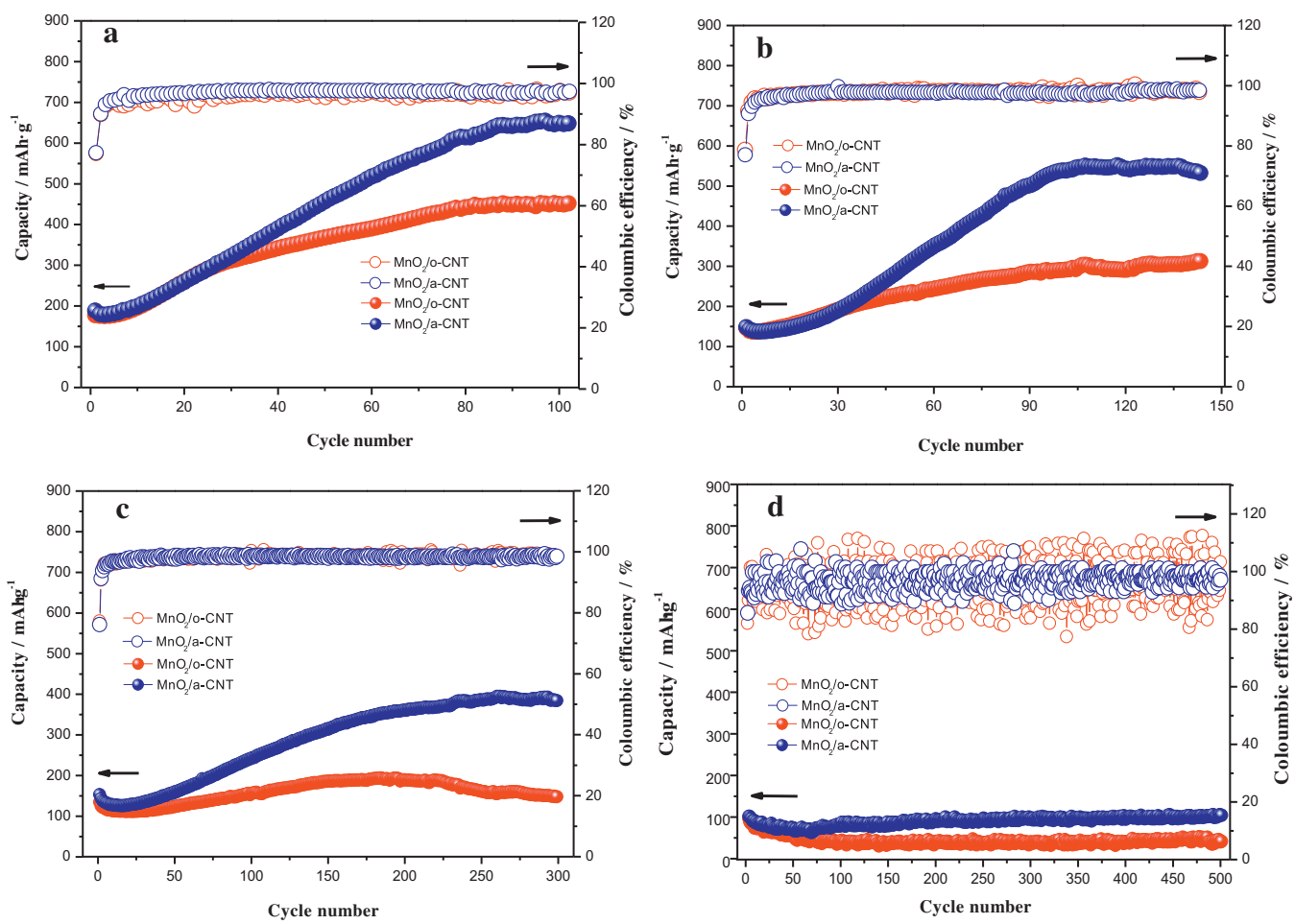

Fig. 6. Cycling performance of the MnO_2/a-CNT and MnO_2/o-CNT electrode in 2 mol·L^{-1} $ZnSO_4$ and 0.5mol·L^{-1} $MnSO_4$ hybrid aqueous electrolyte at the current density of 0.1 A·g^{-1} (a), 0.5 A·g^{-1} (b), 1 A·g^{-1} (c), and 5 A·g^{-1} (d).

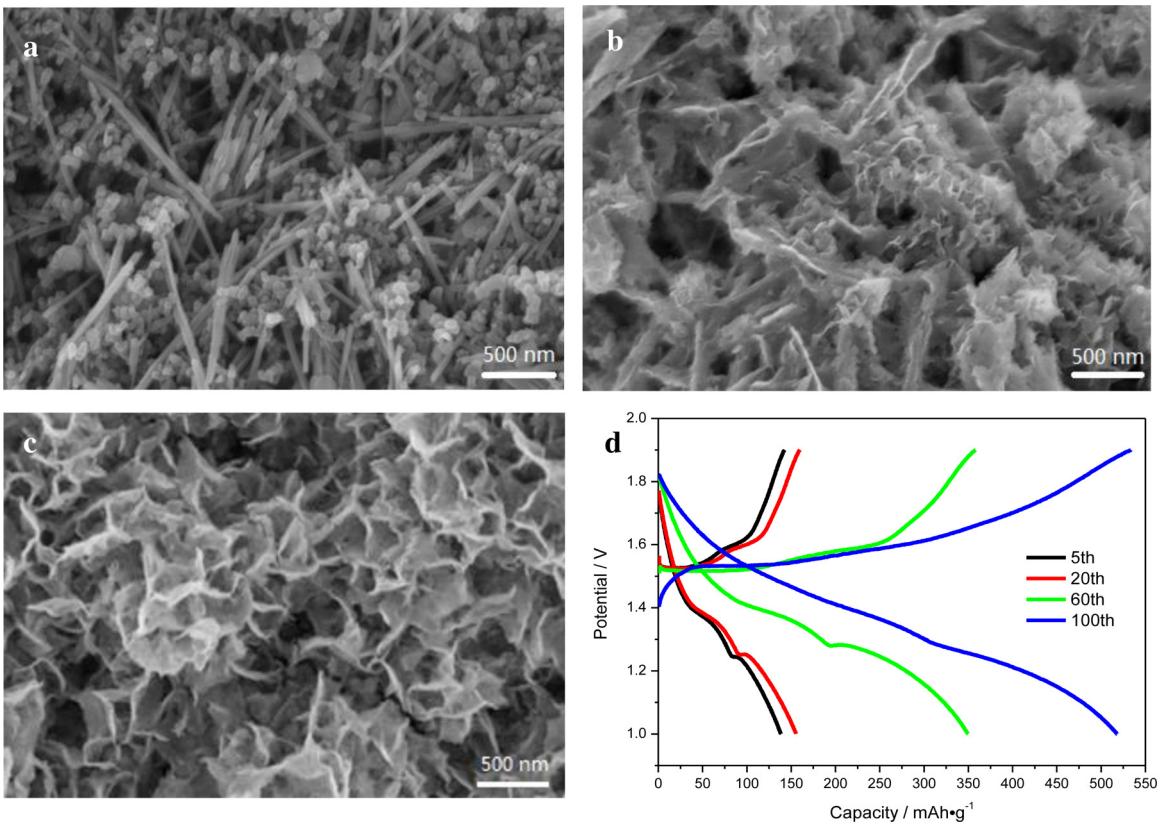

Fig. 7. SEM images of the MnO_2/a-CNT electrode in the original state (a), after 20 time cycle (b) and 100 time cycle (c) at the current density of $0.5A{\cdot}g^{-1}$; charge and discharge profiles of the MnO_2/a-CNT electrode at the current density of $0.5A{\cdot}g^{-1}$ (d).

and hydroxyl group, which is easily combined and tightly connected with MnO_2 to form MnO_2/a-CNT composite with well dispersed CNT and a highly conductive network. This highly electronic network can greatly improve the conductivity of MnO_2, which contributes to the excellent electrochemical performance of MnO_2. Moreover, the presence of CNT with numerous oxidative functional groups can also act as additional lithium storage sites, leading to a dual mechanism of zinc storage and thereby resulting in an improved reversible capacity [38].

Moreover, the specific capacity of the MnO_2/a-CNT electrode gradually increases to higher than the theoretical specific capacity of MnO_2 converted from Mn (IV) to Mn (III). It may be attributed to following possible reasons. Firstly, it is seen from the SEM images of the MnO_2/a-CNT electrode before and after cyclic tests that the MnO_2 has an obviously change from rodlike to flowerlike structure with the increase of cycling number (Fig. 7(a-c)). The flowerlike MnO_2 consisted of nano-sheet and porous structure can increase the utilization of MnO_2 and enable the larger amount of Zn ions storage in the MnO_2 structure. In addition, the formation of MnO_2 nanosheet with porous structure after cycling may result in a large increase of surface area of the MnO_2/a-CNT electrode, which can adsorb and store some zinc ions to form double electrical capacitance. In fact, this capacitance behavior can be observed from Fig. 7(d). It is seen that the slope of charge curve end of the MnO_2/a-CNT electrode gradually decreases with increase of cycle number from 5, 20, 60, to 100 cycles, suggesting an obvious capacitance behavior. Therefore, the MnO_2/a-CNT electrode has higher specific capacity. Besides, the coulombic efficiency was about 100% after 500 cycles at various current densities, indicating a high utility of electric capability. The coulombic efficiency at $5A{\cdot}g^{-1}$, however, have presented slight volatility with the increase of the cycle number, which is due to needing more time to reach electrochemical equilibrium for the MnO_2/a-CNT electrode at high charge/discharge current density.

4. Conclusions

A simple co-precipitation method has been successfully developed to prepare α-MnO_2/a-CNT nanocomposites. The MnO_2 has rod-like structure with the diameter of about 10 nm and length of 50∼120 nm and deposited on the acid-treated CNT's surface. The tests of electrochemical performance of as-prepared MnO_2/a-CNT electrode in the mild aqueous electrolyte ($ZnSO_4$ and $MnSO_4$) revealed that the insertion/extraction mechanism of zinc ions into/from the tunnels of crystalline α-MnO_2 during the energy storage process is different from that of the primary Zn-MnO_2 batteries. Moreover, it is found that the specific capacity of MnO_2/a-CNT firstly increased and then maintained steady after a certain period of time with the increase of cycling number. In particular, their reversible capacity finally maintained stably at $100\ mAh{\cdot}g^{-1}$ even at the high current density of $5A{\cdot}g^{-1}$ and the coulombic efficiency was about 100% after 500 cycles. The excellent reversibility and good cycling properties indicate that the as-prepared MnO_2/a-CNT nanocomposites can be extraordinary promising materials for energy storage devices with desirable energy density.

Acknowledgements

This work was financially supported by the Natural Science Foundation of China (Nos. U1330123 and 51232005), Shenzhen Projects for Basic Research (Nos. JC201005270288A and JC201005310705A), Guangdong Province Innovation R&D Team Plan for Energy and Environmental Materials (No. 2009010025) and National Key Basic Research Program of China (No. 2014CB932400).

Appendix A. Supplementary data

Supplementary data associated with this article can be found, in the online version, at http://dx.doi.org/10.1016/j.electacta.2014.04.001.

References

[1] T. Kousksou, P. Bruel, A. Jamil, Y. Zeraouli, E. Rhafiki, Solar Energy Materials and Solar Cells 120 (2013) 59–80.
[2] Z.M. Dang, J.K. Yuan, S.H. Yao, R.J. Liao, Advanced Materials 25 (2013) 6334–6365.
[3] J.M. Tarascon, M. Armand, Nature 414 (2001) 359–367.
[4] D.Y. Zhai, B.H. Li, H.D. Du, G.Y. Gao, L. Gan, Y.B. He, Q.H. Yang, F.Y. Kang, Carbon 50 (2012) 5034–5043.
[5] C.J. Xu, B.H. Li, H.D. Du, F.Y. Kang, Angewandte Chemie International Edition 51 (2012) 933–935.
[6] C.J. Raj, K.B.R. Varma, Electrochimica Acta 56 (2010) 649–656.
[7] Y. Zhang, H. Liu, Z.H. Zhu, K.W. Wong, R. Mi, J. Mei, W.M. Lau, Journal of Applied Electrochemistry 43 (2013) 705–710.
[8] C.J. Xu, H.D. Du, B.H. Li, F.Y. Kang, Y.Q. Zeng, Journal of the Electrochemical Society 156 (2009) A73–A78.
[9] C.J. Xu, H.D. Du, B.H. Li, F.Y. Kang, Y.Q. Zeng, Electrochemical and Solid State Letters 12 (2009) A61–A65.
[10] D. Aurbach, Z. Lu, Y. Gofer, R. Turgeman, M. Moshkovich, Nature 407 (2000) 724–727.
[11] M. Winter, R.J. Brodd, Chemical Reviews 104 (2004) 4245–4269.
[12] D.Y. Zhai, C.J. Xu, Y.B. He, F.Y. Kang, Journal of Power Sources 196 (2011) 7860–7867.
[13] S.H. Kim, S.M. Oh, Journal of Power Sources 72 (1998) 150–158.
[14] B. Kang, G. Ceder, Nature 458 (2009) 190–193.
[15] C.G. Wei, C.J. Xu, B.H. Li, H.D. Du, F.Y. Kang, Journal of Physics and Chemistry of Solids 73 (2012) 1487–1491.
[16] A.E. Fischer, H.A. Pettigrew, D.R. Rolison, R.M. Stroud, J.W. Long, Nano Letters 7 (2007) 281–286.
[17] Z.Q. Wang, Z.Q. Wu, N. Bramnik, S. Mitra, Advanced Materials 26 (2014) 970–976.
[18] Z.Q. Wang, N. Bramnik, S. Roy, G.D. Benedetto, J.L. Zunino III, S. Mitra, Journal of Power Sources 237 (2013) 210–214.
[19] H. Xia, M.O. Lai, L. Lu, Journal of Materials Chemistry 20 (2010) 6896–6902.
[20] R.K. Sharma, L. Zhai, Electrochimica Acta 54 (2009) 7148–7155.
[21] H. Xia, Y. Wang, J.Y. Lin, L. Lu, Nanoscale Research Letters 33 (2012) 1–10.
[22] J. Sodtipinta, W.P. On, W. Veerasai, S.M. Smith, P. Pakawatpanurut, Materials Research Bulletin 48 (2013) 1204–1212.
[23] Z.Y. Sun, Z.M. Liu, B.X. Han, Y. Wang, J.M. Du, Z.L. Xie, G.J. Han, Advanced Materials 17 (2005) 928–932.
[24] D.K. Walanda, G.A. Lawrance, S.W. Donne, Journal of Power Sources 139 (2005) 325–341.
[25] A.B. Yuan, Q.L. Zhang, Electrochemistry Communications 8 (2006) 1173–1178.
[26] S.L. Kuo, N.L. Wu, Journal of the Electrochemical Society 153 (2006) A1317–A1324.
[27] S. Chen, J.W. Zhu, X.D. Wu, Q.F. Han, X. Wang, ACS Nano 4 (2010) 2822–2830.
[28] F. Aviles, J.V. Cauich-Rodriguez, L. Moo-Tah, A. May-Pat, R. Vargas-Coronado, Carbon 47 (2009) 2970–2975.
[29] C.J. Xu, C.G. Wei, B.H. Li, F.Y. Kang, Z.C. Guan, Journal of Power Sources 196 (2011) 7854–7859.
[30] C.G. Wei, C.J. Xu, B.H. Li, H.D. Du, D. Nan, F.Y. Kang, Journal of Power Sources 234 (2013) 1–7.
[31] C.J. Xu, F.Y. Kang, B.H. Li, H.D. Du, Journal of Materials Research 25 (2010) 1421–1432.
[32] M. Toupin, T. Brousse, D. Belanger, Chemistry of Materials 16 (2004) 3184–3190.
[33] M. Toupin, T. Brousse, D. Belanger, Chemistry of Materials 14 (2002) 3946–3952.
[34] M. Chigane, M. Ishikawa, Journal of the Electrochemical Society 148 (2001) D96–D101.
[35] M. Chen, C.Y. Du, B. Song, K. Xiong, G.P. Yin, P.J. Zuo, X.Q. Cheng, Journal of Power Sources 223 (2013) 100–106.
[36] M. Hu, X.L. Pang, Z. Zhou, Journal of Power Sources 237 (2013) 229–242.
[37] B.H. Li, Y.T. Xing, X.D. Chu, J. Ma, Y.B. He, D.Y. Zhai, H.D. Du, C.G. Wei, H.Z. Chen, F.Y. Kang, International Journal of Electrochemical Science 8 (2013) 446–457.
[38] A.L.M. Reddy, M.M. Shaijumon, S.R. Gowda, P.M. Ajayan, Nano Letters 3 (2009) 1002–1006.